ADVANCED OPTICAL MATERIALS
www.advopticalmat.de

3D Orbital Angular Momentum Nonlinear Holography

*Feiyang Shen, Weiwen Fan, Yong Zhang, Xianfeng Chen, and Yuping Chen**

Orbital angular momentum (OAM), due to its theoretically orthogonal and unbounded helical phase index, is utilized as an independent physical degree of freedom for ultrahigh-capacity information encryption. However, the imaging distance of an OAM hologram is typically inflexible and determined by the focal length of the Fourier transform lens placed behind the hologram. Here, 3D orbital angular momentum holography is proposed and implemented. The Fourier transform between the holographic plane and imaging plane is performed by superimposing Fresnel zone plates (FZP) onto the computer-generated holograms (CGH). The CGH is binarized and fabricated on the lithium niobate crystal by femtosecond laser micromachining. Experimental verification demonstrates the feasibility of the encoding method. Moreover, by superimposing FZPs with different focal lengths into various OAM channels, OAM-multiplexing holograms are constructed. Target images are separately projected to different planes, thereby enabling 3D multi-plane holographic imaging with low crosstalk. The interval between adjacent imaging planes can be uniform and minimal, free from depth of field (DoF) constraints, thus achieving high longitudinal resolution. This work achieves OAM holography in a more compact manner and further expands its applicability.

1. Introduction

Computer-generated holograms utilizing precise amplitude and phase modulation provide an advanced method to design and manipulate complex light fields, including in 3D display,[1–3] image projection,[4] beam shaping,[5,6] and nonlinear holography,[7,8] especially for Fresnel CGH, which can project multiple target images to arbitrary longitudinal position theoretically.[9,10] However, due to the varying depth of field at the corresponding imaging plane, the interval between adjacent imaging planes is non-uniform, with larger intervals at more distant planes, leading to low longitudinal resolution and small capacity, or equivalently, strong crosstalk under the condition of dense image plane distribution (see Note S1, Supporting Information). Orbital angular momentum, as a new physical degree of freedom, has attracted intensive and diverse research interests.[11,12] It is promising in the multiplexing technique due to the orthogonality of its theoretically unbounded OAM modes.[13] In traditional OAM holography, a cumbersome Fourier transform lens is typically placed behind the hologram, resulting in a fixed and inflexible imaging distance for an OAM hologram, thereby limiting its further application.

In this paper, we propose and demonstrate a general approach to realize 3D orbital angular momentum nonlinear holography. By superimposing Fresnel zone plates onto CGHs, Fourier transform operations can be performed within the Fresnel regime,[10] allowing flexible control of the projection depth in OAM holography by adjusting the focal length of the FZPs. Furthermore, the implementation of OAM-multiplexing hologram facilitates the independent control of the projection depth for each OAM channel, leading to the successful realization of low-crosstalk 3D multi-plane imaging. Additionally, this holographic encoding technique obviates the necessity for the Fourier transform lens structure typically required in conventional OAM holography, thereby substantially simplifying the optical configuration. Femtosecond laser micromachining is becoming an advanced method used in various optical research,[14–18] offering an efficient and integrated fabrication approach. The calculated CGH patterns are fabricated in monolithic lithium niobate crystals with binary modulation of quadratic susceptibility by femtosecond laser. Overall, our study contributes to the diversification of implementation methods for OAM holography. It also opens new possibilities for nonlinear multi-plane holography in a single piece of crystal.

2. Result

2.1. Design Principle of 3D OAM Nonlinear Holography

The encoding process of the OAM holography is shown in **Figure 1a**. The target image is first sampled according to the

F. Shen, X. Chen, Y. Chen
State Key Laboratory of Advanced Optical Communication Systems and Networks
School of Physics and Astronomy
Shanghai Jiao Tong University
Shanghai 200240, China
E-mail: ypchen@sjtu.edu.cn

W. Fan, Y. Zhang
National Laboratory of Solid State Microstructures
College of Engineering and Applied Sciences
Nanjing University
Nanjing 210093, China

X. Chen
Collaborative Innovation Center of Light Manipulations and Applications
Shandong Normal University
Jinan 250358, China

The ORCID identification number(s) for the author(s) of this article can be found under https://doi.org/10.1002/adom.202402836

DOI: 10.1002/adom.202402836

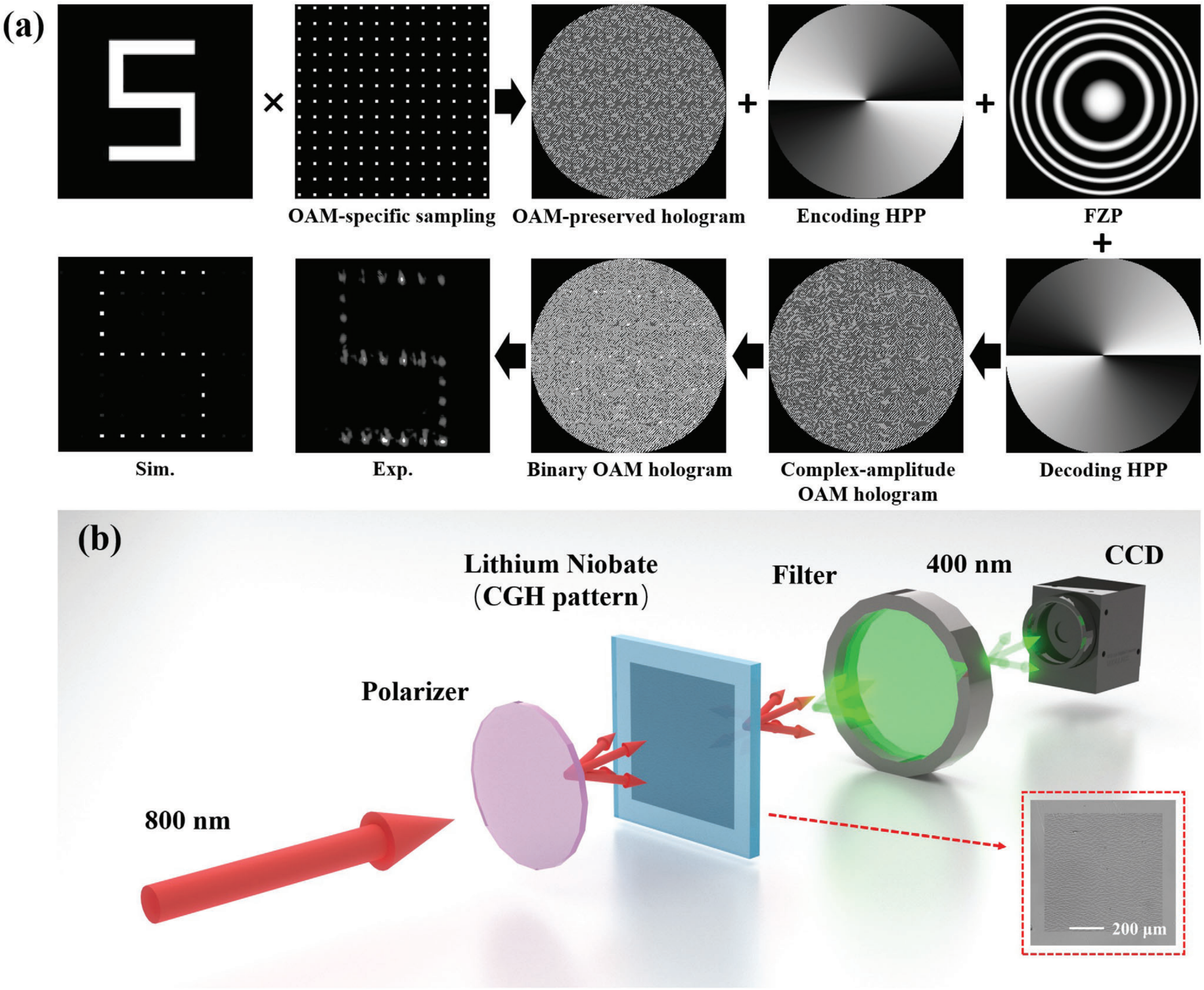

Figure 1. a) Design principle for the OAM hologram; b) Schematic illustration of the optical system for holographic image reconstruction and the optical image of the fabricated hologram on LN sample by femtosecond laser.

spatial frequency of the selected encoding helical phase (see Note S2, Supporting Information). Then, the Gerchberg–Saxton (GS) algorithm is utilized to obtain the OAM-preserved hologram. To construct an OAM-selected hologram, a helical phase plate (HPP) with l_c is encoded onto the OAM-preserved hologram. According to the nonlinear OAM conservation law[19] and nonlinear OAM-matching condition[20] $\Delta l = 2l_w + l_c$, where l_w is the topological charge carried by the incident fundamental beam. The target image can be clearly reconstructed only when an incident OAM beam with $l_w = -1/2l_c$ is used and the reconstructed image consists of pixels that feature Gaussian mode showing high-intensity distribution. On the contrary, if a mismatched OAM beam is incident, each pixel maintains the vortex characteristics and exhibits a lower intensity distribution, which can be regarded as background noise. In this work, a decoding HPP with $-l_c$ is directly superimposed onto the hologram instead of the OAM beam incidence.

In the OAM holography, the electric field on the hologram plane and that on the image plane form a Fourier pair. Direct superposition of a FZP on a Fourier hologram will generate a single-plane Fresnel hologram (see Note S3, Supporting Information), where the focal length of the FZP can be used to translate the image to any distance[10] controllably. Notably, this flexibility is further exemplified by our ability to superimpose Fresnel zone plates with different focal lengths in various OAM channels, thereby projecting different target images onto planes at distinct depths, namely, the 3D multi-plane OAM holography. Meanwhile, the traditional Fourier transform lens structure can be omitted, which greatly simplifies the optical configuration. The phase function of FZP can be written as:

$$\Phi_{FZP}(x, y) = -\frac{k}{2f}(x^2 + y^2) \tag{1}$$

where (x, y) represents the Cartesian coordinates in the holographic plane, k is the wavevector and f represents the focal length. So the final complex-amplitude distribution of an OAM multiplexed hologram can be described mathematically as:

$$U(x, y) = exp(i\Phi_{dec}(x, y)) \sum_{j=1}^{n} E_j(x, y) exp(i\Phi_{j-FZP}(x, y)) exp(i\Phi_{j-enc}(x, y)) \quad (2)$$

where n is the total OAM channel number, $E_j(x, y)$ is the complex-amplitude distribution of the sampled target image obtained by GS algorithm encoded on the j-th OAM channel, $\Phi_{j-enc}(x, y)$ is the phase distribution of the j-th encoding HPP, Φ_{j-FZP} denotes the phase function of the FZP superimposed on the j-th OAM channel and $\Phi_{dec}(x, y)$ is the phase distribution of the decoding HPP. It is worth noting that the depth controllability is achieved by loading different FZP phases onto different OAM channels. It should be emphasized that the size of the reconstructed target image is directly related to the focal length of the FZP. The larger the focal length, the larger the size of the image. Therefore, to achieve a realistic restoration of a 3D object, the images of each plane need to be scaled accordingly in advance (Note S4, Supporting Information).

Finally, we choose a suitable way to encode the complex-amplitude field onto the holographic plane. Considering that we use the femtosecond laser to erase the nonlinear coefficient of the lithium niobate crystal which results in two states corresponding to the actual laser-nonirradiated area and laser-irradiated area, the binary Fresnel CGH was selected in our experiments (see Experimental Section).

Notably, both the FZPs and the binarization process in the encoding process are wavelength-dependent. Therefore, we adopted a configuration where the beam was first frequency-doubled and then modulated, with the design of CGHs specifically tailored for the SH beam. Under the irradiation from the opposite direction, the target image can not be clearly reconstructed(see Note S5, Supporting Information), enabling non-reciprocal information processing. Further, we encode Number "3" and Letter "D" into the OAM channels $l = 0$ and $l = -2$ respectively. If we engrave these two different holograms on the back and front surfaces of the LN crystal separately, the incidence of Gaussian light can reconstruct the Number "3," while the reverse incidence of vortex light with $l = 1$ can reconstruct the Letter "D." Consequently, we can realize that irradiation in both directions will produce different patterns and the capacity of our holography can be further improved by multiplying a factor 2. It is worth noting that this double-layer structure must be based on the laser poling technique to avoid excessive modulation of the fundamental frequency light by the previous layer (see Note S6 for details, Supporting Information).

To validate the effectiveness of this encoding method, the letter S was encoded with a HPP with $l = 4$ and a FZP with $f = 50mm$. When a decoding HPP with $l = -4$ was superimposed onto the hologram, a distinct SH pattern emerged at the corresponding distance with Gaussian-spot pixels under the condition of Gaussian beam incidence, as shown in Figure 1a. The slight difference between the experiment and theoretical simulation is the imperfection of the produced ferroelectric domain structure and the unavoidable random structure errors.

2.2. OAM-Multiplexing Holography at the Same Imaging Plane

The more pronounced difference between the OAM-matching and OAM-mismatching can be demonstrated by constructing an OAM-multiplexing hologram. As can be seen from **Figure** 2a, letters L and N, namely the abbreviation for lithium niobate crystal, were encoded separately into two OAM channels, i.e., $l = 1$ and $l = 3$, while superimposing identical FZPs with $f = 50$ mm projects them onto the same imaging plane. The decoding process can be performed by superimposing corresponding decoding HPP onto the OAM-multiplexing hologram as shown in Figure 2b. Figure 2c,d show the simulation and experimental results, respectively. It is clear that the decoded target image consisted of Gaussian-shaped pixels showing high intensity, corresponding to the OAM-matching condition being satisfied. Due to the OAM mismatching, the other letter had donut-shaped pixels and relatively low intensity, which can be regarded as background noise and can be further removed through post-processing.

2.3. OAM-Multiplexing Holography for 3D Multi-Plane Imaging

Suffering from strong crosstalk and varying DoFs between adjacent planes, it is challenging for traditional 3D holographic imaging techniques to achieve large-capacity and high-fidelity 3D information storage. By leveraging the orthogonality of OAM modes, crosstalk can be significantly reduced, especially since the proposed encryption method now enables precise and independent control over the imaging distances of each OAM channel. Additionally, the intervals between adjacent imaging planes are no longer constrained by the DoFs.

To characterize the 3D reconstruction performance of the proposed OAM holography, we chose multi-plane images of the letters "SJTU" as our 3D object model. As is illustrated in **Figure** 3, the four letters are divided into four layers which are positioned at different distances from the hologram ($z_1 = 42mm$, $z_2 = 43mm$, $z_3 = 44mm$, $z_4 = 45mm$). After performing the GS algorithm, they were separately encoded into four different OAM channels ($l_1 = -3$, $l_2 = -1$, $l_3 = 2$, $l_4 = 4$) and superimposed with corresponding FZPs for independent projection. The OAM-multiplexing hologram was obtained by superposing four DC-OAM-selective holograms. The decoding process is shown in **Figure** 4a. To reconstruct a specific target image, correct decoding HHP should be superimposed onto the OAM-multiplexing hologram. The numerical reconstructions under the Gaussian beam incidence at four different depth planes are shown in Figure 4b–e and the corresponding experimental reconstruction results are shown in Figure 4f–i. After applying a mode-selective aperture array in post-processing of the reconstructed holographic images, most of the OAM-mismatching target images were filtered. To better illustrate the mechanism and the design principle of the mode-selective aperture array, a sample example is presented in Figure S8 (Supporting Information). As we can see, the expected letters appeared at pre-designed distances. Due to inevitable discrepancies between the actual fabricated structures and the designed CGH pattern, the interference between OAM

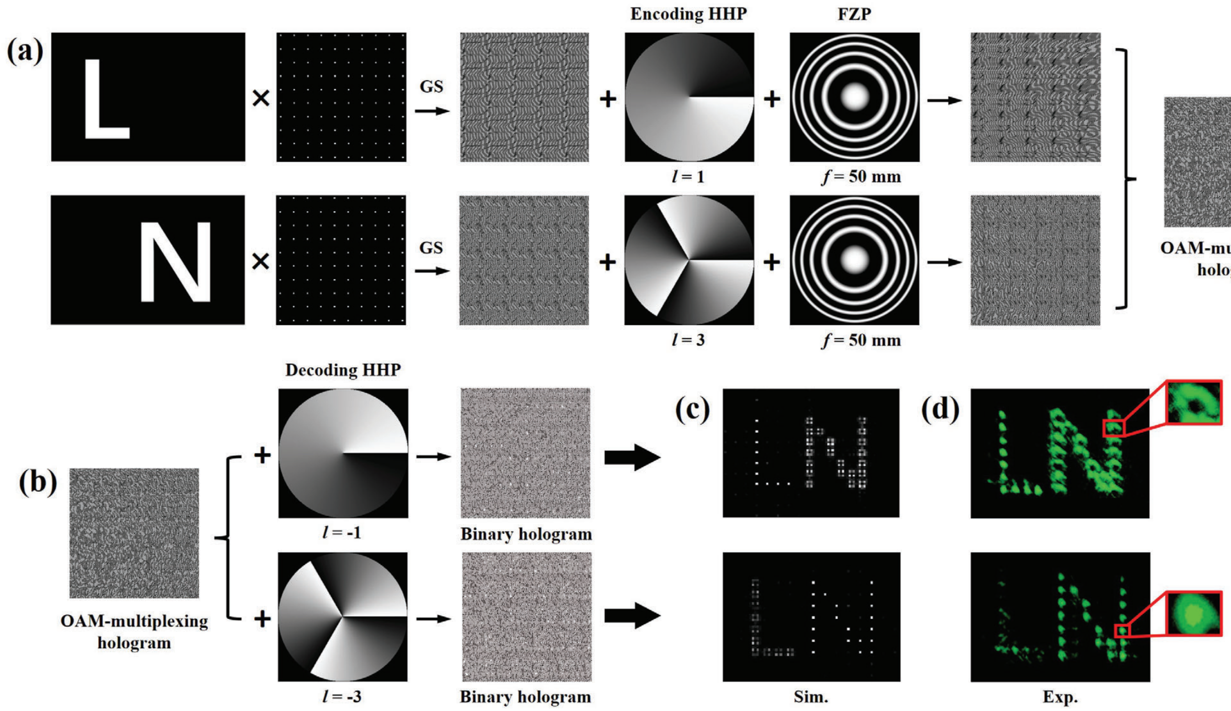

Figure 2. a) Design principle for the OAM-multiplexing hologram with the same depth; b) The decoding process by superimposing corresponding decoding HHP; c) Simulated and d) Experimental reconstruction results at $z = 50mm$.

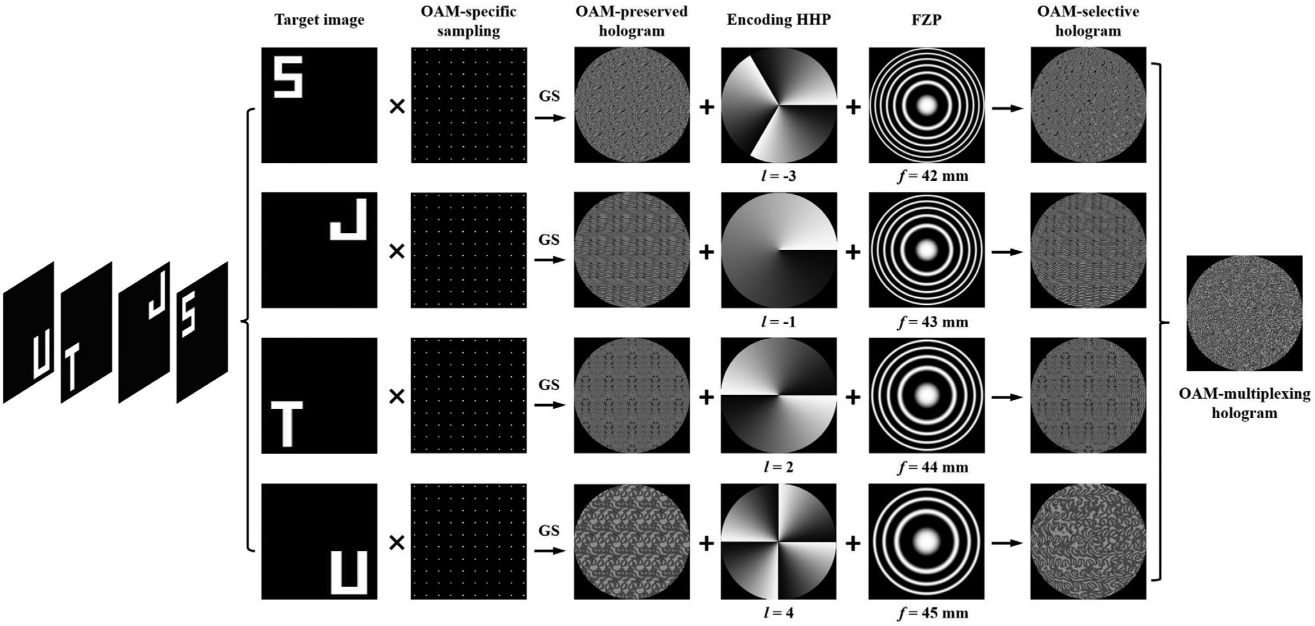

Figure 3. Encoding process of OAM-multiplexing holography for 3D multi-plane imaging. The 3D object "SJTU" is sliced into four planes containing different letters. Each letter is encoded into a distinct OAM channel by applying OAM-specific sampling before performing the GS algorithm and then superimposing with the phase of encoding HHP and FZP. Consequently, four OAM-selective holograms are obtained respectively and then superimposed to construct an OAM-multiplexing hologram.

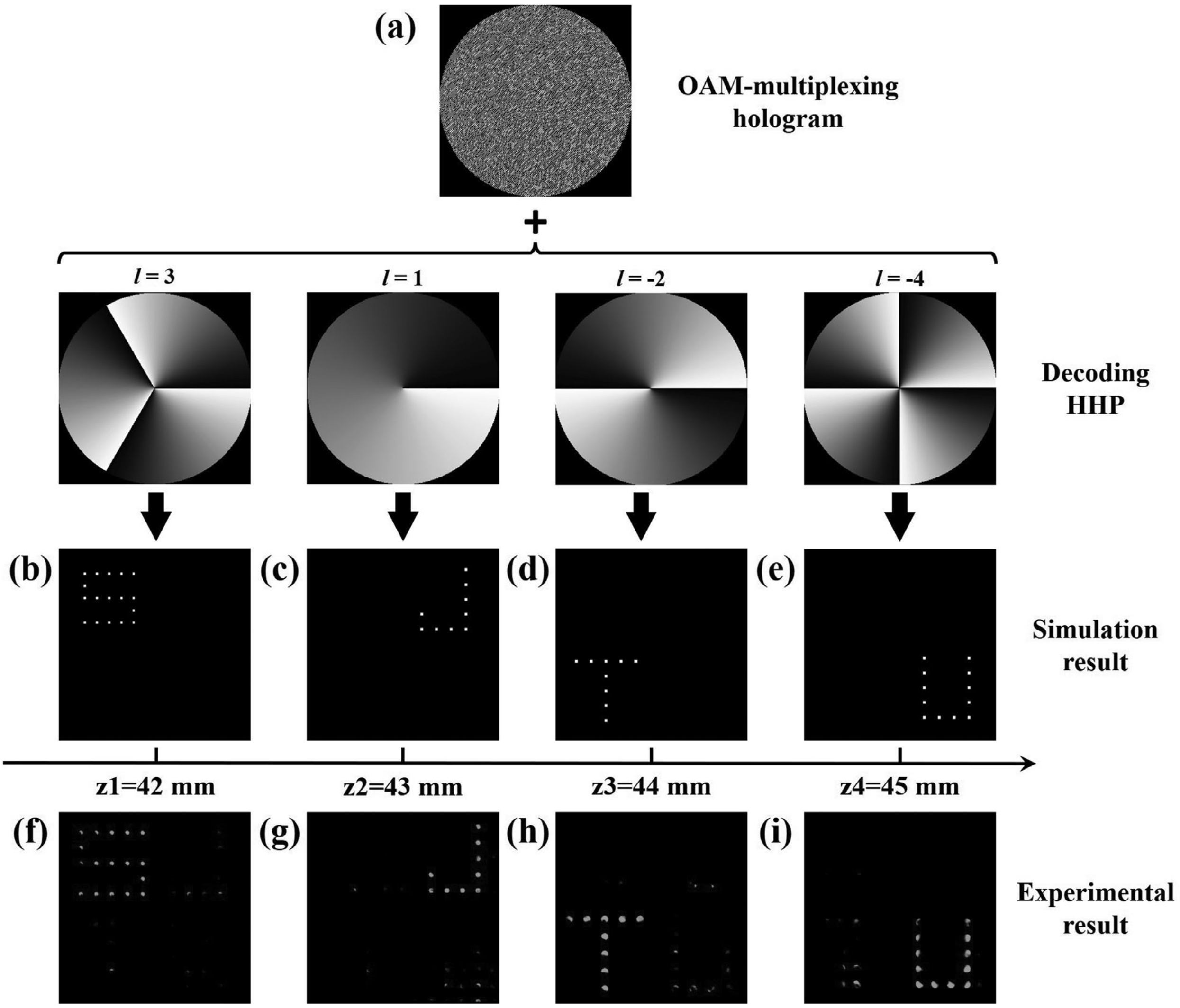

Figure 4. a) Decoding process of OAM-multiplexing holography for 3D multi-plane imaging; b–e) Numerical reconstructions of 3D model "SJTU" at the depth of z1, z2, z3, and z4, respectively; f–i) Experimentally reconstructed images at corresponding positions.

modes in adjacent pixels, termed as adjacent pixel interference (API), is unavoidable. Consequently, high-intensity pixels comparable to those in the signal regions appear in the non-signal areas during experiments, and these pixels cannot be filtered out. Furthermore, a smaller interval of topological charges significantly amplifies the crosstalk between imaging channels, whereas the spacing between imaging planes exerts minimal influence on this phenomenon. A detailed discussion of their respective impacts on crosstalk is provided in Note S8 (Supporting Information).

In order to quantitatively analyze the experimental reconstruction results of our 3D OAM nonlinear holography, the mean square error (MSE) is introduced. It is the average of the squares of the corresponding pixel differences between the numerical and the experimental reconstructed images, which can be expressed as:

$$\mathrm{MSE} = \frac{\sum_{m,n} \left[I(m,n) - I_0(m,n) \right]^2}{M \times N} \tag{3}$$

where $I(m, n)$ and $I_0(m, n)$ represent the optical intensity matrices of experimental and numerical results. M and N are the pixel numbers of matrices corresponding to horizontal and vertical directions. The summation $\sum_{m,n}$ is over all possible pixels with index (m, n) of the image. Generally speaking, a low MSE corresponds to a high-quality reconstruction. We calculate the MSE between the reconstructed and original images. For comparison, random noise images are adopted to calculate the same quantities MSE_0 in which the matrices $I(m, n)$ are replaced by random numbers. The results of MSE and MSE_0 are shown in **Table 1**. It is clear to see that the values of MSE of the reconstructed images are two orders of magnitude smaller than the random noise images, which indicates that the 3D object is well reconstructed by our method.

3. Discussion

The imaging distances and the number of target images selected in this experiment are merely exemplary. In practice, smaller

Table 1. The results of MSE and MSE$_0$.

	Letter S	Letter J	Letter T	Letter U
MSE	0.0028	0.0013	0.0032	0.0047
MSE$_0$	0.3340	0.3358	0.3337	0.3331

distance intervals and a greater number of images can be selected. Both of the transverse resolution and longitudinal resolution, or equivalently the capacity, are constrained by the OAM sampling condition and the numerical aperture of the CCD camera. A larger number of target images necessitates a larger sampling constant. This implies that the target images need to be magnified and a camera with a larger numerical aperture should be used; otherwise, the resolution of the images will degrade, potentially leading to distortion. If our holograms are loaded onto a spatial light modulator and a temporal multiplexing method is employed,[21] this issue can be mitigated. A more detailed discussion of the capacity and resolution is provided in Note S7 (Supporting Information). We compare our 3D nonlinear OAM holography with other reported 3D holography works in terms of capability, resolution, crosstalk, performance and implementation method. As shown in Table S1 (Supporting Information), despite some performance differs, our method shows high resolution, low crosstalk and uniqueness in non-reciprocity. Meanwhile, our encryption method is compatible with other enhanced OAM holography techniques,[21–28] and their integration allows us to further enhance the capacity and resolution of 3D holographic imaging.

In conclusion, we have proposed the concept of 3D OAM nonlinear holography and employed femtosecond laser micromachining technique to fabricate CGH pattern onto the lithium niobate crystal. Our approach utilizes superimposed FZPs in CGH replacing the Fourier transform lens used in the traditional OAM holography, enabling us to flexibly control over imaging distance. Meanwhile, the optical configuration is greatly simplified. Moreover, we constructed OAM-multiplexing holograms to independently project images that loaded in different OAM channels to distinct positions, thereby achieving low-crosstalk 3D multi-plane holographic imaging. Experimental verification has demonstrated the feasibility of 3D OAM nonlinear holography. It is worth mentioning that the proposed OAM holographic encoding strategy represents a universal approach compatible with the majority of OAM holography techniques, holding great promise for applications in various field including 3D display and optical manipulation.

4. Experimental Section

Binarization of the Complex-Amplitude OAM Hologram: To record the information of the complex-amplitude OAM hologram onto the lithium niobate crystal, the method of binary interference CGH was used. Through the interference of the object wave $U(x, y) = A_0(x, y) exp(i\phi_0(x, y)$ and the planar reference wave $R(x, y) = R\exp(i2\pi\alpha x)$, where $A_0(x, y)$ and $exp(i\phi_0(x, y))$ are the amplitude and phase term of the complex amplitude on the holographic plane, R and α are the amplitude and the carrier frequency respectively, the transmittance function $h(x, y)$ of the hologram was obtained first:

$$\begin{aligned} h(x, y) &= |\ U(x, y) + R(x, y)\ |^2 \\ &= \frac{1}{2}\{1 + A_0(x, y)[\cos\phi_0(x, y) - 2\pi\alpha x]\} \end{aligned} \tag{4}$$

The bright fringes equation of the hologram can be obtained as:

$$\phi_0(x, y) - 2\pi\alpha x = 2\pi n \tag{5}$$

where n represents the serial number of the bright fringes, $n = 0, \pm1, \pm2$, ...By solving the position of each bright fringe and opening a thin slit, a binary transmission grating is formed, that is, the phase of the object wave is encoded. The encoding of the amplitude was obtained by introducing an offset $cos\pi q(x, y)$ to modulate the width of the bright fringes,[29] where $q(x, y) = arcsin[Ao(x, y)]/\pi$ and the amplitude $Ao(x, y)$ takes the normalized value. This encoding method is widely used in standard wavefront generation and interference detection.[30,31] Then, the final interference binary CGH is represented as follows:

$$H(x, y) = \begin{cases} 1, & \cos[\phi_0(x, y) - 2\pi\alpha x] \geq \cos\pi q(x, y) \\ 0, & \text{others} \end{cases} \tag{6}$$

Fabrication of CGH by Femtosecond Laser Erasure: The CGH was fabricated using a NIR laser working at 800nm wavelength, 1kHz reputation rate, and 109fs pulse width (Coherent Legend Elite). A 5$mol.\%$ MgO-doped LiNbO3 crystal with a thickness of 1mm was used as a sample which is mounted on the computer-controlled XYZ translation stage with a resolution of 0.2μm. An objective lens with a numerical aperture of 0.90 (Nikon CFI TU Plan Fluor BD) was applied to focus the laser pulse onto the surface of the crystal. The moving speed was 100$\mu m/s$ and the moving direction was perpendicular to the laser beam. In this experiment, a single pulse of about 30μJ was used. Controlled by the computer program, the ferroelectric domain of the crystal was selectively erased corresponding to the dark area of the CGHs. While the non-irradiated points correspond to the white area of the CGHs. The physical mechanism of the ferroelectric domain erasing process can be understood in that the crystallinity is reduced through laser irradiation.[32] The CGH patterns were fabricated with 300 × 300 pixels, where each pixel has a size approximately at 2 μm × 2 μm. The fabricated CGHs were written within an area of 0.6×0.6 mm^2 and the total processing time is 1.5 h.

Experimental Set-up: Figure 1b shows the optical holographic imaging system. The fundamental frequency (FF) beam with a wavelength of 800nm was used for image reconstruction. A linear polarizer was utilized to adjust the polarization of the FF beam. Afterward, an ordinary polarized laser beam was irradiated onto the sample. Given that the CGH pattern was inscribed on the surface of the LiNbO3 crystal, we arranged the sample such that the FF beam initially traversed the unmodulated LiNbO3 crystal, where the second harmonic (SH) beam was generated at the wavelength of 400 nm. Subsequently, the SH beam was modulated by the CGH and projected to the corresponding depth for imaging. Before the CCD camera, a filter was used to separate the FF and SH beams.

Supporting Information

Supporting Information is available from the Wiley Online Library or from the author.

Acknowledgements

This work was supported by the National Natural Science Foundation of China (Grant. 12134009, 12474335, 12192252 and 12425410).

Conflict of Interest

The authors declare no conflicts of interest.

Author Contributions

F.S. and W.F. contributed equally to this work. F.S. prepared the manuscript in discussion with all authors. F.S. and Y.C. designed the holographic method and analyzed the data. F.S. and W.F. fabricated the hologram onto the lithium niobate crystal and performed the experiments. Y.C., X.C., and Y.Z. revised the manuscript. Y.C. supervised the project.

Data Availability Statement

The data that support the findings of this study are available from the corresponding author upon reasonable request.

Keywords

femtosecond laser micromachining, nonlinear holographic imaging, orbital angular momentum

Received: October 20, 2024
Revised: December 27, 2024
Published online:

---

[1] R. G. Dorsch, A. W. Lohmann, S. Sinzinger, *Appl. Opt.* **1994**, *33*, 869.
[2] L. Huang, X. Chen, H. Mühlenbernd, H. Zhang, S. Chen, B. Bai, Q. Tan, G. Jin, K.-W. Cheah, C.-W. Qiu, J. Li, T. Zentgraf, S. Zhang, *Nat. Commun.* **2013**, *4*, 2808.
[3] R. Kang, J. Liu, G. Xue, X. Li, D. Pi, Y. Wang, *Opt. Express* **2019**, *27*, 14369.
[4] M. Meem, A. Majumder, R. Menon, *Appl. Opt.* **2020**, *59*, 38.
[5] M. Manousidaki, D. G. Papazoglou, M. Farsari, S. Tzortzakis, *Opt. Lett.* **2020**, *45*, 85.
[6] B. Zhu, H. Liu, Y. Chen, X. Chen, *Opt. Lett.* **2020**, *45*, 220.
[7] B. Zhu, H. Liu, Y. Liu, X. Yan, Y. Chen, X. Chen, *Opt. Lett.* **2020**, *45*, 4132.
[8] P. Chen, X. Xu, T. Wang, C. Zhou, D. Wei, J. Ma, J. Guo, X. Cui, X. Cheng, C. Xie, S. Zhang, S. Zhu, M. Xiao, Y. Zhang, *Nat. Commun.* **2023**, *14*, 5523.
[9] H. Tu, T. Yuan, Z. Wei, Y. Chen, X. Chen, *Opt. Mater.* **2023**, *135*, 113228.
[10] G. Makey, Ö. Yavuz, D. K. Kesim, A. Turnalı, P. Elahi, S. Ilday, O. Tokel, F. Ö. Ilday, *Nat. Photonics* **2019**, *13*, 251.
[11] X. Fang, X. Hu, B. Li, H. Su, K. Cheng, H. Luan, M. Gu, *Light: Sci. Appl.* **2024**, *13*, 49.
[12] C. Wan, Q. Cao, J. Chen, A. Chong, Q. Zhan, *Nat. Photonics* **2022**, *16*, 519.
[13] X. Fang, H. Ren, M. Gu, *Nat. Photonics* **2020**, *14*, 102.
[14] X.-J. Wang, H.-H. Fang, Z.-Z. Li, D. Wang, H.-B. Sun, *Light: Sci. Appl.* **2024**, *13*, 6.
[15] Y. Wang, L. Zhong, K. Y. Lau, X. Han, Y. Yang, J. Hu, S. Firstov, Z. Chen, Z. Ma, L. Tong, K. S. Chiang, D. Tan, J. Qiu, *Light: Sci. Appl.* **2024**, *13*, 130.
[16] Z.-Z. Li, L. Wang, H. Fan, Y.-H. Yu, Q.-D. Chen, S. Juodkazis, H.-B. Sun, *Light: Sci. Appl.* **2020**, *9*, 41.
[17] S. Liu, L. M. Mazur, W. Krolikowski, Y. Sheng, *Laser Photonics Rev.* **2020**, *14*, 2000224.
[18] H. Zhu, L. Chu, W. Liu, S. Juodkazis, F. Chen, *Adv. Opt. Mater.* **2023**, *11*, 2300929.
[19] X. Hu, Y. Zhang, S. Zhu, *Adv. Mater.* **2020**, *32*, 1903775.
[20] X. Fang, H. Wang, H. Yang, Z. Ye, Y. Wang, Y. Zhang, X. Hu, S. Zhu, M. Xiao, *Phys. Rev. A* **2020**, *102*, 043506.
[21] Z. Shi, Z. Wan, Z. Zhan, K. Liu, Q. Liu, X. Fu, *Nat. Commun.* **2023**, *14*, 1869.
[22] P. Cheng, S. Huang, C. Yan, *JOSA A* **2021**, *38*, 1875.
[23] G. Zhu, Z. Bai, J. Chen, C. Huang, L. Wu, C. Fu, Y. Wang, *Opt. Express* **2021**, *29*, 28452.
[24] F. Wang, X. Zhang, H. Yuan, R. Xiong, X. Jiang, *IEEE Photonics J.* **2022**, *14*, 1.
[25] F. Wang, X. Zhang, R. Xiong, X. Ma, X. Jiang, *Opt. Express* **2022**, *30*, 11110.
[26] F. Li, S. Nie, J. Ma, C. Yuan, *Opt. Express* **2022**, *30*, 41567.
[27] F. Li, H. Ding, S. Nie, J. Ma, C. Yuan, *Opt. Lasers Eng.* **2023**, *160*, 107303.
[28] N. Zhang, B. Xiong, X. Zhang, X. Yuan, *Adv. Photon. Nexus* **2023**, *2*, 036013.
[29] W.-H. Lee, *Appl. Opt.* **1974**, *13*, 1677.
[30] J. Wyant, V. Bennett, *Appl. Opt.* **1972**, *11*, 2833.
[31] J. H. Burge, in Int. Conf. Opt. Fabric. Test., vol. *2576*, SPIE, **1995**, pp. 258–269.
[32] D. Wei, C. Wang, H. Wang, X. Hu, D. Wei, X. Fang, Y. Zhang, D. Wu, Y. Hu, J. Li, S. Zhu, M. Xiao, *Nat. Photonics* **2018**, *12*, 596.